Bioprinting 52 (2025) e00457

Contents lists available at ScienceDirect

Bioprinting

journal homepage: www.sciencedirect.com/journal/bioprinting

Reseach paper

Development of an on-demand foaming printhead for biofabrication of constructs with heterogeneous porosity

Mohammadamin Zohourfazeli [a,c], Pakshid Hosseinzadeh [b,c], Elias Madadian [a,c], Sara Badr [a,c], Sophie Lerouge [a,b,c], Ali Ahmadi [a,c,*]

[a] Department of Mechanical Engineering, École de technologie supérieure (ÉTS), Montreal, QC, Canada
[b] Department of Radiology, Radio-Oncology and Nuclear Medicine, Université de Montréal, Montreal, QC, Canada
[c] Biomaterials and BioFabrication Laboratory, Centre de recherche du Centre hospitalier de l'Université de Montréal (CRCHUM), Montreal, QC, Canada

ARTICLE INFO

Keywords:
3D bioprinting
Macroporous bioinks
Printhead
Albumin
Sodium alginate
Foam

ABSTRACT

Cell scaffolding and metabolic exchange are critical in tissue engineering and drug delivery applications, where porosity plays a crucial role in facilitating nutrient diffusion and waste removal. To tackle the challenge of biofabricating heterogeneous constructs, this study focuses on developing 3D bioprinted tunable macroporous scaffolds with a range of pore sizes. The approach utilizes the rapid cross-linking of sodium alginate via calcium chloride mist and the on-demand foaming capability of albumin within a printhead. The pore diameter is controlled by adjusting the foaming speed during printing, enabling the biofabrication of heterogeneous structures. The study examines the effects of various foaming speeds (1500, 2500, and 3500 rpm) on printability, water content, degradation, drug release, and biocompatibility properties of foams made from a bioink containing 2 % (w/v) sodium alginate, 2 % (w/v) albumin, 2 % (w/v) gelatin. At lower foaming speeds, larger pore sizes result in higher water content, degradation, and drug release due to larger pores facilitating higher water intake, quicker degradation, and shorter drug diffusion pathways. The proposed technique demonstrated excellent printability, layer adhesion, and shape fidelity, with a printability number over 0.90. A passive cell mixer was added to the foaming printhead, leading to cell-laden printed scaffolds. Fibroblast L929 cells exhibited over 90 % viability after 24 h according to the Live/dead assay, highlighting the biocompatibility of the system.

1. Introduction

Tissue engineering has advanced to address the challenges posed by the increasing rate of tissue degeneration and the vulnerability to injuries associated with rapid global aging [1,2]. The development of porous biomaterials is crucial in this field, as non-porous structures exhibit inadequacies in nutrient supply, oxygen transport, and waste material removal [3]. Additionally, porosity facilitates the delivery of bioactive compounds and offers suitable surfaces that promote cell proliferation and differentiation [4]. The optimal pore size varies depending on cell type and application: it ranges from 20 to 125 μm for adult mammal skin regeneration [5], 100–400 μm in bone tissue engineering [6], and in the order of 100 μm for vascularization purposes [7]. However, the porosity of many biomaterials is generally much smaller than these values and may not always meet these specific requirements due to their inherent structure and composition. Thus, developing methods to fabricate supermacroporous biomaterials with precise control over pore characteristics is essential for targeted applications [8].

The methods of fabrication of porous biomaterials can be categorized into two main approaches: i) kinetic methods, such as gas injection [9], freeze-drying [10], and gas foaming [11]; and ii) templating methods, including solid-phase templating [12] and foam-templating [13,14]. The resulting pore diameters vary depending on the technique used, ranging from 10 to 1000 μm for gas injection, 10–200 μm for freeze-drying, and less than 10–1000 μm for foam templating [13]. Key concerns with these pore-generation methods include the use of toxic gases or solvents, the poor properties of the porous construct, the lack of control over desired pore characteristics, and the ability to create cell-laden porous constructs [13]. Therefore, it is essential to develop pore-generation methods that facilitate cell incorporation and precise control over pore characteristics while minimizing the use of detrimental additives and complex processing steps. Among foam templating methods including protein foams [15], polymer hydrogel foams [16],

* Corresponding author. Department of Mechanical Engineering, École de technologie supérieure, Montreal, QC, Canada.
E-mail address: ali.ahmadi@etsmtl.ca (A. Ahmadi).

https://doi.org/10.1016/j.bprint.2025.e00457
Received 2 July 2025; Received in revised form 6 November 2025; Accepted 25 November 2025
Available online 27 November 2025

and synthetic polymer biofoams [17,18], protein foams are widely used due to foam stabilization of proteins as a function of pH, temperature, and ions, while offering a more biocompatible and viable foaming process [15,19]. Whipping proteins induces structural denaturation, creating hydrophobic and hydrophilic groups that trap gas within the solution, leading to the formation of foamed porous constructs. Incorporating surfactants can enhance foamability and stability during the whipping process; however, this may negatively impact cellular activities. Critical concerns with foams include phase separation and variation in the properties of biomaterials across different batches, which can affect cell distribution and mechanical properties.

Three-dimensional (3D) bioprinting techniques are used to create complex porous structures through the systematic deposition of bioink onto a printing surface, guided by a digital model [20,21]. To fabricate porous scaffolds, 3D bioprinting has been combined with various approaches, including conventional methods such as freeze-drying [10] or batch foaming applied to fused deposition modeling [22,23]. However, these techniques require either extremely low or high temperatures during the fabrication process, making them incompatible with cell encapsulation and thus necessitating that cells be seeded at later stages [22,23].

An alternative approach involves the use of micro-mesh filters to entrap air bubbles in the bioink to fabricate porous hydrogels [24–26]. In this method, the bioink is forced through a micro-mesh during extrusion, enabling foam generation during printing. However, although mesh-based bubble entrapment enables in situ pore formation, the resulting air bubble size is primarily determined by the mesh geometry, and therefore does not allow on-demand modulation of porosity during the fabrication of heterogeneous scaffolds.

Among other various methods, another emerging approach is combining mechanical foaming of protein-based hydrogels, such as albumin [27], silk-fibroin [14], and gelatin methacrylate (GelMA) [28], with 3D bioprinting to enable the fabrication of porous biomaterials with compatible properties. For instance, Madadian et al. recently introduced an innovative approach that passively prepares foam bioink for 3D bioprinting using a crosslinker mist delivery system [27], where porous hydrogels were created by leveraging the foaming ability of albumin and the rapid ionically crosslinking of hydrogels.

However, such techniques require preparing the porous hydrogel precursors prior to printing [29], where the material is foamed externally and then loaded into the 3D printer and then mixed with cells. These pre-formed foams are often unstable due to the high surface tension at the air–liquid bubble interface, resulting in bubble coalescence or collapse during printing. Furthermore, they do not allow porosity to be dynamically adjusted in real time during printing, which limit fabrication of constructs with spatially heterogeneous or gradient pore architectures, that are often required to replicate native tissue microenvironments. Additionally, maintaining a uniform distribution of pores within the structure remains a challenge, particularly when it comes to ensuring consistent cell placement. Therefore, the development of in-situ foaming printheads can significantly enhance the capabilities of 3D bioprinting systems for on-the-fly adjustment of the pore sizes during the printing process.

In this article, a newly designed printhead was developed to foam an albumin/alginate-based bioink while 3D bioprinting. The foam porous structure was preserved by using a calcium chloride mist delivery system during 3D bioprinting. By adjusting the foaming speed, pore size, consequently, the structural and mechanical properties can be modified without the need for surfactants. The hypothesis proposes that this foaming printhead could produce versatile bioprinted scaffolds with tunable functionality, adaptable to various applications and cell types.

2. Experimental section

2.1. 3D printing setup

The foaming printhead was designed by using 3D CAD software (Solidworks, Dassault Systems) and includes three modules of foaming, mixing, and crosslinking (Fig. 1a). Details of these modules are provided in the following sections. The foaming printhead is assembled onto a commercial 3D printer (A1 Mini, Bambu Lab, China), as it is mounted with a few modifications (Video 1). The positioning system independently controls movements in all axes using stepper models. 3D printing was performed at a speed of 10 mm/s, which was optimized to allow stable deposition of the bioink; higher speeds resulted in filament dragging, nozzle clogging, and reduced shape fidelity.

2.1.1. Foaming module

The foaming module includes a DC motor (3–12V, Sntieecr) covered with a motor lock and closure (Fig. 1c). The motor lock is a single component divided into two sections by a wall. One section is longer and provides space for securing the motor, featuring inner threading that matches the outer threading of the cap for securely holding the motor. The other section allows the motor shaft to enter through a hole in the wall, which is sealed by an O-ring. A connection part featuring a central hole accommodates the motor shaft and includes a side shaft. A pinion is designed with a hole on one side to fit onto the connection part, which allows its proper rotation in the space enclosed by an annular cap. The annular cap component features internal teeth that facilitate the rotation of the pinion within it to induce high shear forces on the fluid to initiate foaming. The annular cap is threaded on the outside and fits the inner threading of the upper part of the motor lock. An O-ring, fitting at the bottom of the foaming space, seals this area. The annular cap includes two inlets for air and bioink. The bioink was loaded in a syringe and introduced into the printhead using a syringe pump set to a flow rate of 0.35 ml/min. The inlet air pressure was maintained at 1.8 psi using a pressure regulator (Model 700, ControlAir, USA). The pinion is made of PLA by a commercial 3D printer (Ender-3 S1 Pro), and the rest of the parts were fabricated using a Formlabs printer with grey resin. Furthermore, three foaming speeds of 1500, 2500, and 3500 rpm were used, which were optimized to create foams with the desired bubble size (50–200 μm).

2.1.2. Mixing module

The mixing module is a sterile, passive cell mixing unit (KT0000000000, CELLINK) with two inlets (one for the foam and one for the cell suspension) and an outlet for the cell-laden foam. The inlets have separate channels that meet in the central section of the cell mixer, where the components are blended by passing through helical blades. A syringe pump is used to push the cell suspension into the mixer. A luer lock needle gauge of 20 with a 1/2 mm length was chosen to avoid clogging. The inner diameter of the needle was set as the layer height of the printed structure.

2.1.3. Crosslinking module

The needle is secured in a crosslinking module customized based on a previously developed system []. An ultrasonic atomizer was placed into a container containing a calcium chloride solution to produce mist and delivered to the crosslinking module using an air pump [30]. This module was 3D printed using a Formlabs printer with grey resin. The module includes two separate inner channels, one inlet for crosslinker mist and the other for collecting the excess mist using a vacuum pump (Fig. 1d). The internal geometry of the crosslinking module was optimized to manage the mist flow during both delivery and removal. The inlet leads to a space at the bottom of the device, which narrows down to a small opening around the needle tip. This setup allows the mist droplets to flow around the bioink stream, creating a stream of mist. Excess mist droplets are then pulled towards a small opening near the

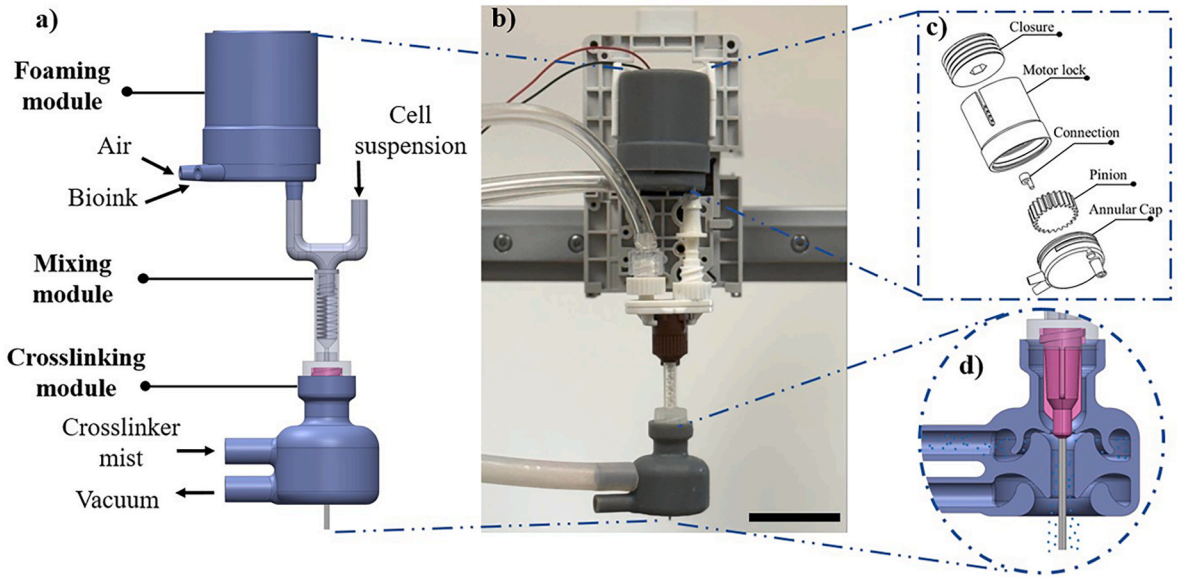

Fig. 1. On-demand foam 3D bioprinting system. a) Full CAD view showcasing 3 modules of foaming, mixing, and crosslinking with the associated inlets and outlets. b) 3D bioprinting printhead mounted onto a 3D printer. c) Close-up view of components of the foaming module (closure, motor lock, connection, pinion, and annular cap). d) Cross-sectional CAD view of the crosslinking module. (Scale bar: 30 mm).

outer edge of the base.

2.2. Preparation of bioink and crosslinker

Bioinks with 2 % sodium alginate and various albumin concentrations were prepared to fabricate heterogeneous macroporous constructs (Table 1). Alginate provided the printable matrix, albumin enabled foam stabilization, and gelatin (when used) improved cell adhesion and extrusion stability. Gelatin-containing inks were printed at room temperature to avoid premature gelation. The albumin concentration range was selected based on previous findings [27]; lower albumin concentrations yield unstable foams, whereas higher concentrations become too viscous and are difficult to foam using mechanical mixing. The bioinks were prepared by adding sodium alginate powder (W201502; Sigma-Aldrich, USA) in HEPES (pH: 7.4) at 1000 rpm for 5 h. Subsequently, egg albumin (9761, McCall's, CA, USA) was dissolved in the solution by stirring at 700 rpm for 2 h. Gelatin type B (G9391, Sigma Aldrich, USA) at a final percentage of 2 % w/v was added to the bioink at 37 °C and 700 rpm for 2 h to increase cell attachment and bioink viscosity. To prepare a calcium chloride solution (20 % w/v), $CaCl_2$ in granular form (1023782500; Sigma-Aldrich, USA) was added to DI water and stirred at 500 rpm for 4 h.

2.3. Porosity assessment and SEM imaging

Foams were prepared at various foaming speeds (1500, 2500, and 3500 rpm) using the printhead. A thin layer of foam samples was collected on a Petri dish to characterize the size of the bubbles under transmitted light microscopy (RVL-100-G, Echo Laboratories, San Diego, CA). Three images were captured from random locations of the samples to investigate the effect of foaming speed on pore size. The diameter of 150 bubbles from each sample was measured. The measurements were rounded to the nearest μm and reported, as the level of uncertainty was calculated to be 1 μm. Filaments (5 mm) at various foaming speeds were freeze-dried after 1 day of air drying at room temperature to characterize their cross-section features by SEM (TM3000; Hitachi, Japan) [27]. The freeze-dried samples were coated with gold (thickness: 300 Å), and the SEM imaging was conducted at 15 kV in analysis mode.

Table 1
Name and composition of the various bioinks (S: Sodium Alginate, A: Albumin, G: Gelatin).

Bioink	Sodium Alginate (% w/v)	Albumin (% w/v)	Gelatin (% w/v)
S2A2	2	2	–
S2A3	2	3	–
S2A4	2	4	–
S2A8	2	8	–
S2A2G2	2	2	2

2.4. Printability

The printability and layer adhesion of the proposed printhead were examined by printing Y-shape, star-shape, and grid scaffolds using the following printing parameters: printing speed of 10 mm/s, bioink flow rate of 0.35 ml/min, air pressure of 1.8 psi, and needle gauge of 20. Printability number (Pr) was evaluated using two-layer grid scaffolds featuring a 2 × 2 cm grid CAD model with 15 % infill. Images were analyzed using an image processing software (Fiji, ImageJ) to calculate the printability number, and the uncertainty of the printability measurements was calculated to be 0.04. The ideal printability number is 1, corresponding to perfectly squared grid pores, and a printability number closer to 1 indicates better printability. The printability number is defined as

$$\mathrm{Pr} = \frac{L^2}{16\,A}, \tag{1}$$

where L is the perimeter of the pore between filaments and A is the area of the mentioned space [31].

Foam filament collapse tests were conducted using samples produced at three different foaming speeds (1500 rpm, 2500 rpm, and 3500 rpm) to investigate their time-dependent deflection characteristics [32]. A custom platform with 2 mm wide supports was designed and fabricated using a Creality Ender-3 S1 Pro 3D printer. The distance between supports (gap, L) was varied at 2, 4, 8, and 16 mm. Foam samples were directly printed onto the platform using the respective foaming speeds. The deflection of foam samples was recorded using a Canon PowerShot SX740 HS compact camera at a frame rate of 25 frames per second (fps). Image analysis was performed using the image processing software, ImageJ, to measure the maximum deflection of each foam sample at different gap sizes for up to 10 s, or until no further movement was

observed.

2.5. Water content and degradation

Grid-patterned and ten-layered 2 × 2 cm scaffolds with 15 % infill were 3D-printed and incubated in HEPES. For the water content test, after submerging samples for 30, 60, and 90 min, upon removal of media after incubation, samples were dried at 37 °C for 1 day. The weight of the wet scaffold after incubation (W_2) and the dried scaffold (W_1) were used for water content calculation [27]. For the degradation test, the dry weight (W_i) of the samples was obtained through freeze-drying of the samples right after printing. To obtain degraded weight (W_d), samples were submerged in HEPES and incubated for 6 and 24 h at 37 °C. The media was pipetted out of the incubated samples, and the samples were freeze-dried and weighed (W_d) [33]. Water content and degradation rate of the filaments were calculated for triplicates of each sample by equations (2) and (3), respectively as

$$\text{water content} = \frac{W_2 - W_1}{W_1} \times 100, \tag{2}$$

and

$$\text{degradation} = \frac{W_i - W_d}{W_i} \times 100. \tag{3}$$

2.6. Drug release

Rhodamine B, as a model drug, was incorporated into the scaffolds to evaluate the drug release rate of the 3D-printed scaffolds. Rhodamine B was added to the bioink (sodium alginate 2 %, albumin 2 %, and gelatin 2 % w/v) and mixed at 700 rpm for 2 h. Subsequently, 5 cm-long filaments were fabricated and crosslinked using the same 3D printing parameters described previously. These scaffolds were immediately immersed in 30 mL of phosphate-buffered saline (PBS) with a pH of 7.4 (VWRL0119; VWR, USA), serving as the dissolution medium. The medium was continuously stirred at 100 rpm at 37 °C.

One milliliter of the dissolution medium was sampled at 10, 20, 30, 60, 120, 180, and 240 min, and each time, it was replenished with an equivalent volume of fresh PBS. The release of rhodamine B was measured using a UV–Vis spectrophotometer (Cary 100; Agilent, USA) at the lambda max of rhodamine B (554 nm), and the cumulative release (%) was calculated accordingly.

2.7. Filament swelling and spreading ratio

Foam filaments were fabricated using three distinct foaming speeds: 1500 and 3500 rpm. The diameter of each filament was measured immediately after printing (D_0). Each filament had a length of 30 mm. Subsequently, the filaments were immersed in 3 mL of HEPES buffer for predetermined time intervals of 30, 60, and 90 min at 37 °C. At the end of each interval, the immersion medium was removed, and the filament diameter was remeasured (D_t).

The swelling percentage (S) was calculated as the relative increase in diameter compared to the initial diameter, using equation (4):

$$\text{S}\ (\%) = \frac{D_t - D_0}{D_0} \times 100 \tag{4}$$

Additionally, the **spreading ratio** (SR) was determined to assess the extent of filament expansion **immediately after exiting the nozzle**. The spreading ratio was calculated as the ratio of the extruded filament width (W) to the nozzle diameter (D), using Equation (5):

$$\text{SR} = \frac{w}{D} \tag{5}$$

2.8. Mechanical property characterization

The mechanical properties of the hydrogels were evaluated through unconfined compression tests performed on a MACH-1™ Micromechanical Testing System (Biomomentum, Laval, Canada) equipped with a 100 N load cell. Approximately 1 mL of hydrogel was deposited layer by layer using the foaming system into cylindrical molds (14 mm in diameter × 10 mm in height) and incubated at 37 °C for 24 h to ensure complete gelation and structural stabilization.

Compression was applied vertically until 80 % strain was reached, at a constant strain rate of 100 % min^{-1}. Engineering stress was calculated by dividing the applied force by the initial cross-sectional area of each sample. The resulting stress–strain curves were used to determine the secant modulus at 10 % strain (from the linear region between 0 and 10 %) and to record the maximum stress at 80 % strain for comparison among the sample groups.

2.9. Cell culture and viability

Bioinks were prepared after exposure of ingredients to ultraviolet (UV) light for 30 min under a biological hood. HEPES and calcium chloride solution were filtered through a 0.22 μm pore size filter for sterilization (Millipore® Steritop®, Merck KGaA, Darmstadt, Germany). The scaffolds were 3D printed by sterilized printheads and printing equipment to avoid contamination.

The bioink composed of sodium alginate 2 %, albumin 2 %, and gelatin 2 % w/v (S2A2G2) was chosen for the cell study. Gelatin was added for its well-known cell-adhesive properties to avoid the intrinsic limitations of the alginate in terms of cell attachment. Mouse fibroblasts L929 – Passage 7 to 13 – were seeded at 2000 cells/cm2 on T175 tissue culture flasks (Canted Neck Red Ventilated Cap for Adherent Cells, 50-809-259, SARSTEDT Inc.) and cultured up to 90 % confluence before the experiment in a humidified incubator (37 °C and 5 % CO_2) in DMEM supplemented with FBS (10 % $v.v^{-1}$) and penicillin/streptomycin (1 % $v.v^{-1}$). Right before cell mixing, the cells were detached with 0.03 mL/cm^2 of Trypsin/EDTA (Wisent) and incubated for 3 min in culture media to stop the negative effect of trypsin. The solution was centrifuged in 50 ml tubes at 500 g for 5 min. Then, concentrated cells were re-suspended in complete media at 10 folds of the designated encapsulated cell concentration, 3 million cells per milliliter, and added to the bioink before printing.

Cell viability experiments were conducted on non-foam samples, samples foamed by the foaming printhead at 1500 and 2500 rpm, and samples foamed by a mechanical mixer (RK-50006-01, Cole-Parmer®) at 2500 rpm for 10 and 130 s. All bioinks were exposed to $CaCl_2$ mist during extrusion. After printing, the crosslinked cell-laden structures were exposed to crosslinker mist for a further 3 min to ensure proper crosslinking. The structures were immersed in a DMEM pool for 5 s to remove the remaining unreacted $CaCl_2$ from the structures. Then, they were cultured in a humidified incubator with culture media for nutrient delivery. Sufficient and consistent nutrient delivery to the cells was provided by changing the cell culture media on day 1. Live/Dead assays were performed to determine the effect of the process on the cell viability and to determine if the change in the pore size has any effect on cells compared to the non-foamed ink. The bioink composition and the details of the experiments are summarized in Tables 2 and 3.

The first study evaluated the viability of cells without using the cell-mixing module: the cell-laden bioink was directly foamed either using the foaming printhead or the mechanical mixer (Table 2). Viability was tested at day 1. In the second study, a sterile passive cell mixing unit (CELLINK) was used to mix foam and cell solution (Table 3), and viability was studied at days 1 and 3.

Live/dead: Cells were stained with fluorescents dyes - Calcein, AM (Invitrogen, Life Technologies, Carlsbad, CA, USA) at a concentration of 2 μM and Ethidium Homodimer-1 (EthD-1, Invitrogen, Life Technologies, Carlsbad, CA, USA) at a concentration of 5.5 μM in DEMEM serum

Table 2
Various study groups, associated bioink composition, foaming system, process, and speed associated with the first cell viability study (S: sodium alginate; A: Albumin and G: gelatin).

Group number	Bioink composition	Foaming system	Process	Foaming speed (rpm)
1	S2A2G2	No foaming	Step i: Crosslinking of bioink droplets	–
2		Foaming printhead	Step i: Foaming cell-free bioink in the foaming module	1500
3			Step ii: Crosslinking of the foam by the crosslinking module	2500
4		Mechanical mixer	Step i: 120 s foaming cell-free bioink Step ii: Addition of cells Step iii: 10 s foaming cell-laden foam Step iv: Crosslinking foam droplets	2500
5			Step i: 130 s foaming cell-laden bioink Step ii: Crosslinking foam droplets	2500

Table 3
Various study groups, associated bioink compositions, foaming system, process, and speed associated with the second cell viability study (cells added to foam using the passive mixing module) (S: sodium alginate; A: Albumin and G: gelatin).

Group number	Bioink Composition	Foaming system	Process	Foaming speed (rpm)
6	S2A2G2	Foaming printhead	Step i: Foaming cell-free bioink in the foaming module	1500
7			Step ii: Mixing foam and cell in the mixing module Step iii: Crosslinking of the foam by the crosslinking module	2500
8		No foaming	Step i: Crosslinking	–
9	S2G2		the bioink droplets	–

free were used as per the manufacturer's protocol – and remained in a humidified incubator for 45 min. After staining, samples were washed with serum-free DMEM and imaged using a fluorescence microscope (RVL-100-G, Echo, San Diego, CA, USA) at random locations of samples. The result of this assay was analyzed using image processing software (Fiji, ImageJ) by counting the number of red (dead) and green (live) signals. The cell viability percentage was calculated as [34].

$$\text{Cell viability } \% = \left(1 - \frac{\text{Dead cells}}{\text{All cells}}\right) \times 100. \quad (5)$$

2.10. Statistical analysis

Statistical analysis of the data was conducted using Analysis of Variance (ANOVA). In all tests, statistical significance was attributed to *p*-values less than 0.05. To compare data between each pair of groups, a Tukey post hoc analysis was employed. All reported results are presented as mean values along with their respective standard deviations, and all tests were performed in triplicate for robustness and consistency.

3. Results and discussion

3.1. Porosity assessment

S2A2G2 was selected for further characterization among the other compositions according to the osmolarity values (Appendix 1). The porous foam was successfully created within the foaming module of the printhead. Fig. 2a depicts microscopic and bright field SEM images of foams (S2A2G2) produced at various foaming speeds of 1500, 2500, and 3500 rpm. The bubble sizes decrease as the foaming speed increases, where the average bubble size is 96, 84, and 53 μm at speeds of 1500, 2500, and 3500 rpm, respectively. Higher foaming speeds cause the fluid to experience greater shear forces, which 1) prevents bubbles from coalescing into larger ones and 2) breaks larger bubbles into smaller ones. In other words, more energy is imparted into the system, which is sufficient to overcome the surface tension forces. Moreover, higher foaming speeds decrease pore size and also result in a more uniform size distribution. At 3500 rpm, the pores are the smallest and possess a more uniform size distribution, while at 1500 rpm, the pores are larger, and less uniformity in size distribution is observed (Fig. 2b). This can be attributed to more efficient dispersion of air in the solution at higher shear rates. The highly porous inner morphology of two foam filaments (S2A2G2) foamed at 3500 rpm, positioned next to each other, is observed in Fig. 2c. The cross-sectional view of the foam filament depicts the moderately interconnected pores. Fig. 2d shows a 3D-printed filament with variable average bubble size obtained by decreasing the foaming speed from 3500 to 1500 rpm (top to bottom) during printing. This feature provides the user with the capability to bioprint heterogeneous porous structures, transitioning back and forth from one porosity to another.

3.2. Printability analysis

A series of shapes and 2 × 2 cm grids were fabricated from S2A2G2 and crosslinked with 20 % $CaCl_2$ (S2A2G2-CC20), to assess and showcase layer adhesion, shape fidelity, and printability using the foaming printhead. Fig. 3a presents the computer model of the grids, 3D printed multi-layer/crosslinked grids, a series of shapes (Cube, Y-shape, star-shape), a non-crosslinked grid, and geometrical parameters used for printability analysis. All samples showed proper layer adhesion and shape fidelity, except the non-crosslinked grid, indicating the necessity of crosslinking. Strong layer stacking and adhesion were evident when the 10-layer grid was suspended from the corner immediately after printing. This showcases that layer adhesion was achieved by the partial crosslinking upon exiting the needle, in addition to the mist exposure while printing. In the 3D printed star shape, the filaments exhibit merging at the corners while the filament throughout the rest of the structure is consistent and printed with high resolution. The Y-shape held its form well, demonstrating decent dimensional accuracy; however, there was extra material buildup on the left arm and a rounded finish rather than a clean intersection where the arms join the main stem. This could be due to factors such as print speed and over-extrusion. However, at the tip of the two upper arms, a merging of the filaments and a slight geometrical inaccuracy is observed. Various 2-layered grids are provided in Fig. 3b to investigate the effect of crosslinking, foaming speed, albumin reduction, and addition of gelatin. Comparing the grids and filament width (*x*-*y* plane), gelatin-containing samples demonstrated more geometrical accuracy. Samples containing gelatin, crosslinked with 15 % and 20 % w/v $CaCl_2$ (CC15 and CC20), demonstrated a promoted gelation as the filament diameter is more uniform in all foaming speeds compared to the samples without gelatin (crosslinked with 15 % w/v $CaCl_2$). Moreover, less filament merging is observed where two filaments intersect/overly in gelatin-containing samples compared to the ones without gelatin. The observed spread and diameter inconsistency across the filaments in samples without gelatin (S2A8) can be attributed to high albumin concentration, which hinders

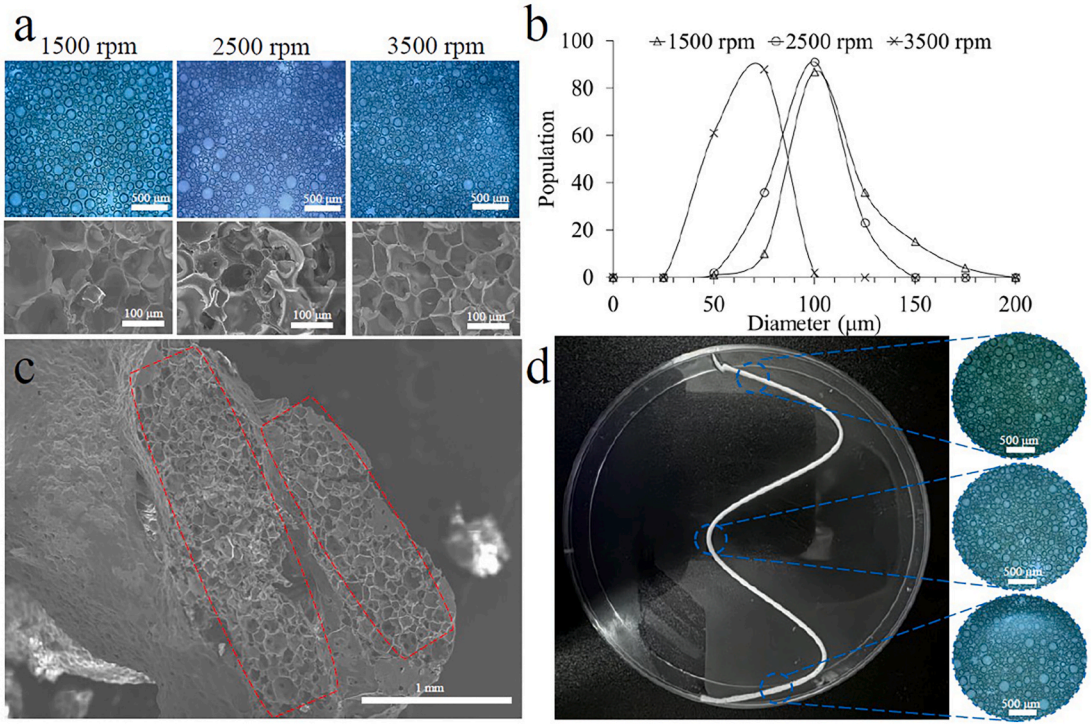

Fig. 2. Physical characterization of foams (S2A2G2). a) Images of bubbles immediately after foaming at 1500, 2500, and 3500 rpm. b) Size distribution of bubbles foamed at various speeds. c) Cross-section and surface SEM images of a filament foamed at 3500 rpm (after lyophilization and gold sputtering). d) An S2A2G2 filament printed while decreasing the foaming speed (top to bottom, 3500, 2500, 1500 rpm on-demand to increase the average bubble size distribution (top to bottom, 53, 84, and 96 µm).

proper crosslinking. Lowering the albumin content decreases osmolality, which enhances the interactions between the crosslinking agents and the biopolymers, leading to improved mechanical properties and reduced filament spread. Comparing samples with the same composition (S2A2G2) but exposed to different crosslinker concentrations (15 % and 20 % w/v) indicates promoted gelation and uniform formation of filaments in all foaming speeds by increasing crosslinker concentration. Comparing filament merging with a focus on overlaying spots shows less merging in samples crosslinked with 20 % w/v $CaCl_2$.

Quantified results are shown in Fig. 3c. Gelatin-containing samples (S2A2G2-CC15 and S2A2G2-CC20) foamed at various foaming speeds exhibited printability numbers above 0.90. According to a previous study on passive foaming and 3D bioprinting, a bioink composition with 2 % sodium alginate and 8 % albumin (w/v), crosslinked with 10 % calcium chloride (w/v), was identified as an optimal printable composition compared to samples with lower albumin concentration [27]. However, the printability number reported in that study was below 0.90. This bioink showed low printability with the on-demand foaming printhead. Consequently, in this study, the crosslinker concentration was increased from 10 to 15 % to enhance crosslinking by delivering additional crosslinking agents. Nonetheless, the results of the S2A8-CC15 sample group exhibited printability numbers below 0.90 at all foaming speeds.

The higher printability observed in S2A2G2-CC15 compared to S2A8-CC15 can be attributed to the addition of gelatin, which compensated for the reduction in albumin concentration that otherwise would decrease printability. A previous study has reported lower printability in samples with reduced albumin concentration. Madadian et al. concluded that foams with higher albumin concentration demonstrate greater stability, firmness, and printability [27]. In this study, however, higher albumin concentrations improved foamability and spread, causing breakage of the connection part in the foaming module of the printhead. These findings highlight the significance of optimizing albumin concentration to achieve high printability and shape fidelity.

Increasing the $CaCl_2$ concentration from 15 % to 20 % w/v raised the printability number for samples foamed at 1500, 2500, and 3500 rpm. Printability improved from 0.92 ± 0.01, 0.97 ± 0.01, and 0.91 ± 0.01 to 0.95 ± 0.02, 0.99 ± 0.02, and 0.96 ± 0.01 for structures foamed at 1500, 2500, and 3500, respectively. This result suggests that fine-tuning the crosslinker concentration to deliver an adequate number of crosslinking agents is essential. For S2A2G2-CC15 and S2A2G2-CC20, the printability number was significantly higher at 2500 rpm compared to 1500 rpm and 3500 rpm ($^*p < 0.05$). At 2500 rpm, the foaming process may achieve an optimal balance between uniformity and stability for these groups. Higher or lower rpm values (1500 or 3500) could lead to less optimal mixing, either due to insufficient energy (at 1500 rpm) or excessive shear force (at 3500 rpm). In contrast, in the S2A8-CC15 group, the printability number was lower at 2500 rpm than at 1500 rpm and 3500 rpm; however, this difference was not statistically significant.

The filament collapse test showed no filament sagging as the gap between pillars increased from 2 mm to 16 mm (Fig. 3d). This was observed in samples containing 2 % w/v sodium alginate, 2 % w/v albumin, and 2 % w/v gelatin foamed at 1500, 2500, and 3500 rpm. The filament deflection is influenced by the crosslinking level of the filament and its weight between two pillars [34]. The consistent performance across different pillar gaps re-confirms that the on-demand filament crosslinking was sufficient to support its structural stability and prevent sagging due to weight difference.

3.3. Water content and degradation

The water content of foam scaffolds (S2A2G2-CC20) produced at different foaming speeds (1500, 2500, and 3500 rpm) over 30, 60, and 90 min are depicted in Fig. 4a. Higher water content is observed in samples foamed at lower speeds at each timepoint. Samples foamed at 1500, 2500, and 3500 rpm demonstrated 3210 ± 144 %, 2224 ± 129 %, and 1733 ± 63 % water content after 30 min, respectively. This can be

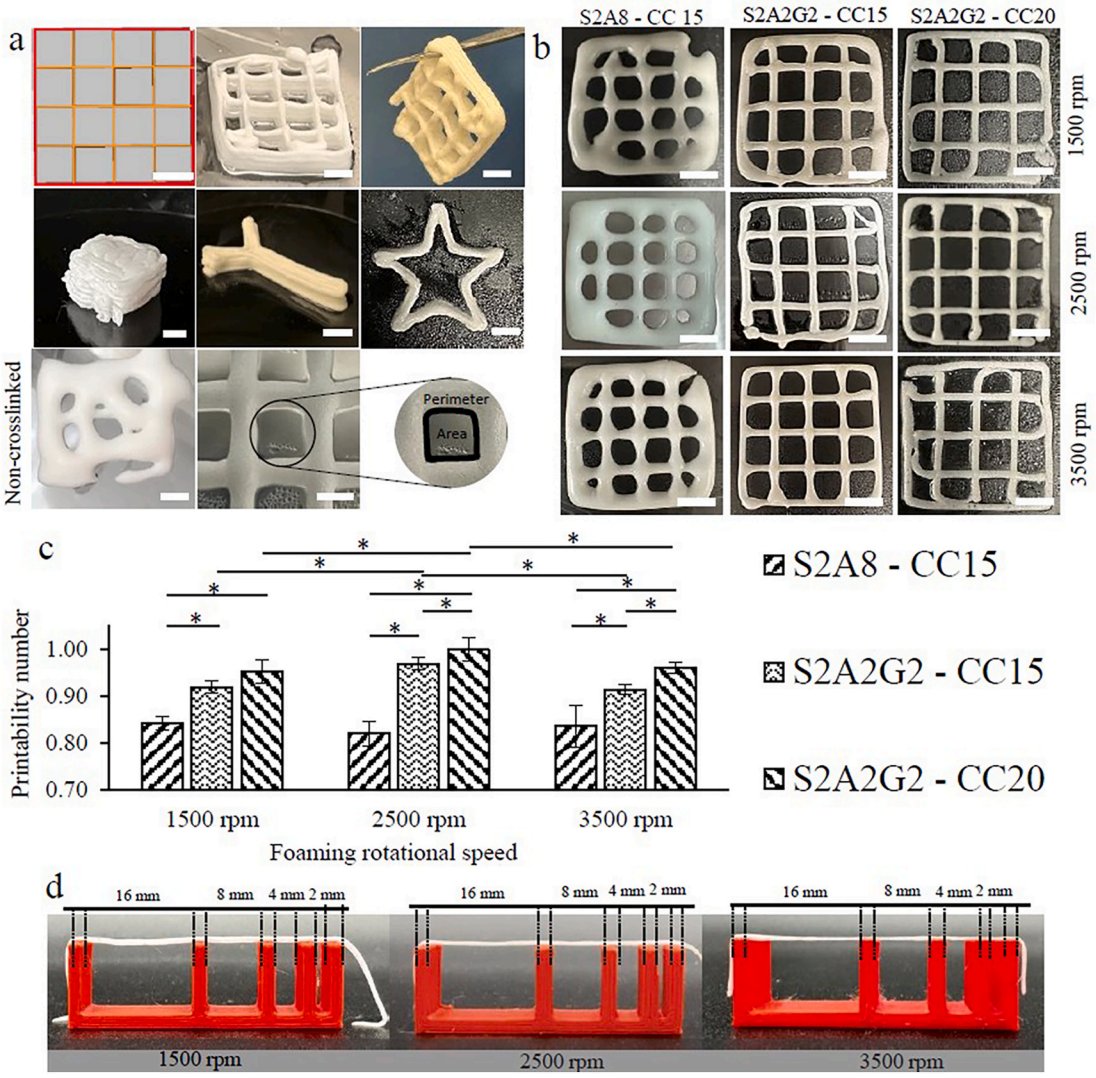

Fig. 3. Printability assessments. a) Computer model of the grids, 3D printed series of crosslinked structures, non-crosslinked grid, and geometrical parameters used for printability analysis. b) 3D printed 2-layer grids foamed at 1500, 2500, and 3500 rpm. c) Printability number of various bioinks. d) Filament collapse test-Snapshots of foam filaments (S2A2G2) foamed at various speeds. (Scale bar: 0.5 mm, calcium chloride concentration (CC), $^{*}p < 0.05$).

related to bubble size measurements: lower foaming speeds create larger inner bubbles and surface pores [30]. These larger surface pores can absorb more media due to the higher osmolality of the foam compared to the media. As the media penetrates the structure, it fills the cavities left by gelatin that melts and is released at 37 °C. Afterward, the media flows toward the bubbles connected to the cavities. Water absorption continued to slightly increase with time. Thus, foam produced at 1500 rpm showed 3210 ± 144 %, 3445 ± 32 %, and 3493 ± 72 % after 30, 60, and 90 min, respectively. This trend correlates with the swelling of constructs as the diffused water breaks down chemical bonds, so the material degrades, pores merge, and more water is absorbed [27].

The degradation profile of the foam, expressed as the percentage of dry weight lost after immersion in HEPES for 6 and 24 h (Fig. 4b), follows the same trend as the water content. Samples foamed at 1500 rpm presented degradation percentages of 70.31 ± 1.88 % and 72.92 ± 9.26 %, after 6 and 24 h, respectively. These values were recorded as 57.52 ± 2.70 % and 64.34 ± 4.99 % for samples foamed at 2500 rpm, and 27.23 ± 2.77 % and 35.52 ± 4.22 % for samples foamed at 3500 rpm. The difference was more pronounced for the foams produced at 3500 rpm ($^{*}p < 0.05$ at each timepoint with the 2 others). This can be explained by the larger difference in pore size compared to 1500 and 2500 rpm. This suggests that higher pore size enhances the degradation. In agreement with previous studies [35], as incubation time increases, the material undergoes prolonged exposure to environmental conditions to break pore walls and promote degradation.

In agreement with the water content results, the higher diffusion of media into larger surface pores leads to higher media intake within the bubbles. In addition, higher release of gelatin into the media causes an increase in degradation. The inverse relationship between rotational speed and degradation suggests that controlling pore size through foaming parameters can be an effective strategy for tailoring material stability in various biomedical applications where controlled degradation is paramount [36].

3.4. Drug release characterization

The cumulative release profiles of the rhodamine B from the foams (S2A2G2-CC20) produced at three different foaming speeds (1500, 2500, and 3500 rpm) are depicted in Fig. 4c. The release was monitored for 6 h. The results indicate a rapid initial release phase followed by a plateau, suggesting a burst release followed by a release stop in all samples. Samples foamed at higher speeds showed less cumulative drug release. For the samples foamed at 1500 rpm, the cumulative release reached 80.10 ± 5.84 %, 87.38 ± 1.13 %, 89.38 ± 1.33 %, and 97.20 ±

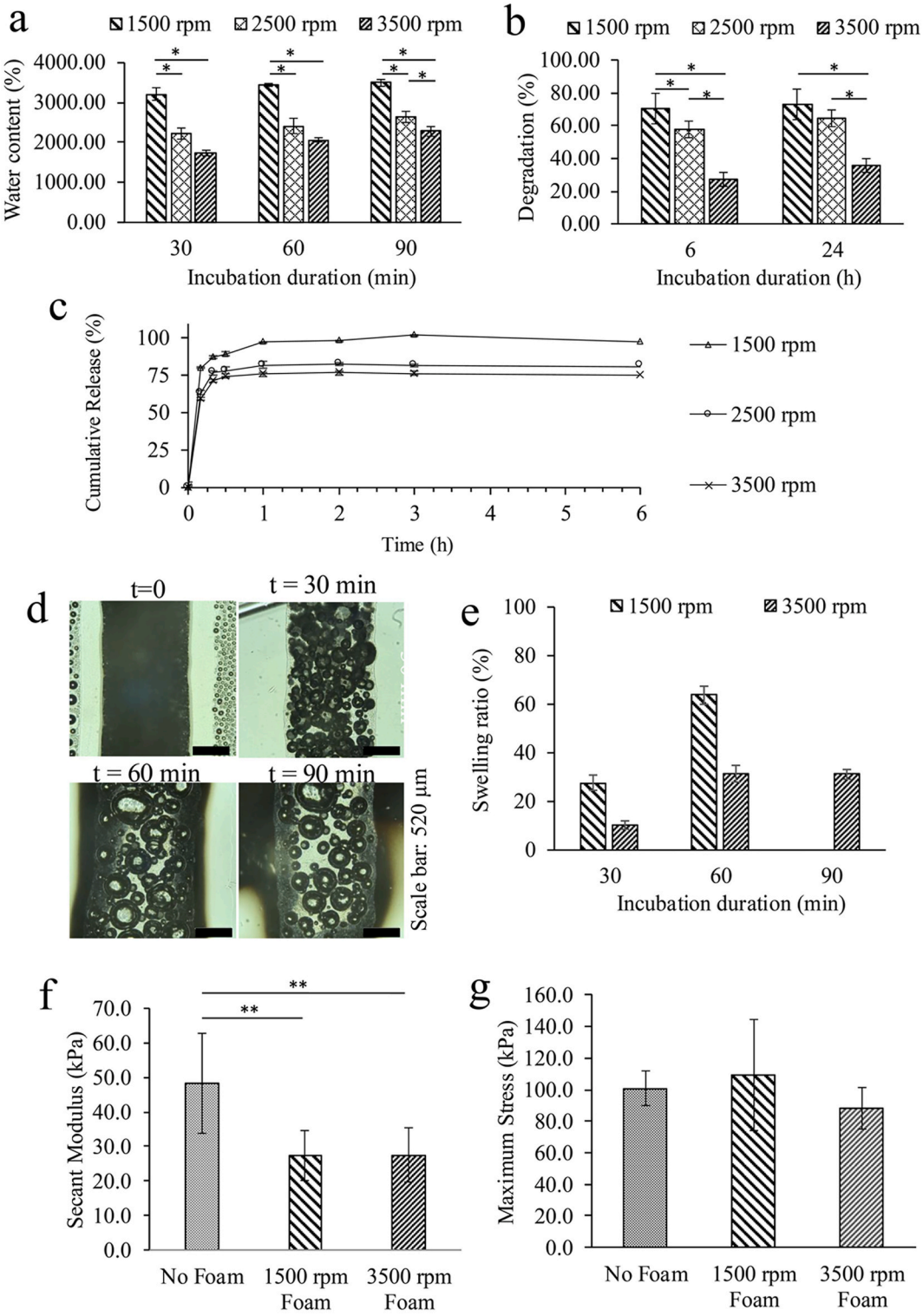

Fig. 4. a) Water content, b) degradation, and c) rhodamine B release of foams (S2A2G2-CC20) produced at various foaming speeds of 1500, 2500, and 3500 rpm (*$p < 0.05$). d) Swelling behavior of foam filament produced at 3500 rpm immediately after 3D printing (0, 30, 60, and 90 min of incubation at 37 °C; scale bar: 520 µm). e) Swelling ratio of foam filaments produced at 1500 and 3500 rpm (30, 60, and 90 min of incubation at 37 °C. f) Secant modulus and g) maximum stress at failure for non-foamed hydrogels and hydrogel foams produced at 1500 rpm and 3500 rpm (**$p < 0.01$).

2.18 % within 10, 20, 30, and 60 min and maintained this level throughout the 6 h. The samples foamed at 2500 rpm exhibited a lower initial release of 63.51 ± 0.84 % after 10 min, which increased to 82.06 ± 3.42 after 60 min and remained constant afterward. The samples prepared at the highest foaming speed of 3500 rpm showed the lowest initial release of 59.59 ± 2.41 % after 10 min, which also plateaued at 60 min and maintained this release level throughout the study. Since material breakdown is faster in foams with larger pore sizes, which correlates with water content and degradation results, drug release occurs rapidly. Moreover, due to larger pores, the shorter release pathways in these samples cause higher release rates. As mentioned in previous literature [27], the release characteristics of bioinks are affected by the

crosslinking method, their concentration, and the duration of exposure. Rapid drug release from filaments is associated with rapid loss of structural integrity due to the presence of gelatin in the structure and its rapid melting at 37 °C.

3.5. Swelling ratio

The swelling behavior of foam filaments (S2A2G2-CC20) produced at 1500 and 3500 rpm was evaluated over 30, 60, and 90 min of incubation (Fig. 4d–e). At all time points, filaments produced at 1500 rpm exhibited higher swelling ratios compared to those produced at 3500 rpm. After 30 min, the swelling ratio of 1500 rpm filaments was approximately 27 %, compared to 10 % for 3500 rpm filaments. This trend continued at 60 min, with their swelling ratio increasing to 63 % and 31 % respectively. After 90 min, the swelling ratio for 1500 rpm filaments could not be measured due to complete structural disintegration, while 3500 rpm filaments maintained a swelling ratio of approximately 31 %. These results indicate that lower foaming speeds promote higher swelling, consistent with the larger pore size and more open structure formed at lower speeds.

The lower swelling observed in 3500 rpm filaments can be attributed to their smaller pore size, which restricts media uptake and limits overall swelling capacity. In contrast, the larger pores formed at 1500 rpm provide more space for water absorption, resulting in greater swelling. These findings are consistent with water content and degradation results, which demonstrated higher media absorption and faster degradation in samples produced at lower foaming speeds. As with other processes in these foams, swelling behavior is directly influenced by the balance between pore size and structural stability, highlighting the importance of controlling foaming speed to achieve tailored properties for specific applications.

The spreading ratios of the filaments, immediately after exiting the nozzle, for 1500, 2500, and 3500 rpm were 1.59 ± 0.01, 1.32 ± 0.01, and 1.22 ± 0.01, respectively. As the foaming speed increased, the spreading ratio decreased, indicating reduced filament expansion after extrusion. This inverse relationship suggests enhanced printability at higher foaming speeds by minimizing filament widening. A low spreading ratio, approaching 1, is desirable for fabricating well-defined, high-resolution hydrogel constructs [37,38]. This trend aligns with previous studies, where PEGMA-based bioink, with the highest spreading ratio (6.06 ± 1.60), exhibited the poorest printability, whereas GelMA, with the lowest spreading ratio (1.43 ± 0.36), ensured more consistent filament formation. Similarly, alginate (3.35 ± 0.93) and agarose (2.58 ± 1.06) exhibited intermediate spreading ratios, correlating with moderate printability [38].

3.6. Mechanical characterization

As can be seen in Fig. 4f, introducing on-demand foaming resulted in a clear reduction in stiffness compared to the non-foamed hydrogel. The secant modulus at 10 % strain decreased from 48.3 ± 14.6 kPa in the non-foamed condition to 27.3 ± 7.3 kPa and 27.5 ± 7.7 kPa for the 1500 rpm and 3500 rpm foamed samples, respectively. The non-foamed hydrogels exhibited a significantly higher modulus than both foamed groups ($p < 0.01$), while no statistically significant difference was observed between the two foaming speeds. This reduction in modulus is consistent with the increased porosity introduced during foaming, which reduces the effective load-bearing cross-section and allows greater deformation under compression. The similarity in modulus between 1500 rpm and 3500 rpm suggests that, within this polymer formulation and crosslinking regime, the presence of pores is the dominant factor controlling stiffness, whereas the differences in pore size between the two foaming speeds are not sufficient to produce measurable mechanical divergence.

In contrast, as can be seen in Fig. 4g, the maximum stress at failure did not vary significantly among the three conditions, with measured values of 100.8 ± 10.8 kPa (No Foam), 109.3 ± 34.9 kPa (1500 rpm), and 88.0 ± 13.3 kPa (3500 rpm). Notably, this occurs despite the non-foamed gels containing a more continuous alginate network. One explanation is that the degree and uniformity of $CaCl_2$ crosslinking achieved via mist exposure may differ between dense and foamed constructs. In foamed samples, the aerated structure likely enhances mist penetration and Ca^{2+} diffusion, enabling more homogeneous ionic gelation throughout the volume. Meanwhile, in the non-foamed hydrogel, Ca^{2+} transport during gelation may be more restricted to the outer regions, producing a gradient in crosslink density. As a result, the effective crosslinking efficiency across the sample volume may be comparable across conditions, leading to similar ultimate strength even though the network architectures differ.

3.7. Cell viability

3.7.1. Impact of foaming method, speed, and time

For ease of reference, the compositions of all formulations used in this section are summarized in Tables 1–3, which outlines the alginate/albumin/gelatin ratios and corresponding printing conditions. In a first experiment, the effects of the foaming method, speed, and time on cell viability were assessed within five sample groups. The control group (group 1) is the crosslinked cell-laden S2A2G2-CC20 bioink without foaming. In groups 2 and 3, the cell-laden bioink was foamed at 1500 and 2500 rpm by the foaming printhead. In groups 4 and 5, foaming was carried out by a mechanical mixer at 2500 rpm. The key difference between groups 4 and 5 was the timepoint, at which the cells were added to the bioink. In group 4, the bioink was foamed for 120 s, after which the cells were added, and the cell-laden bioink was foamed for an additional 10 s. In group 5, the cell-laden bioink was foamed for the entire 130 s.

As shown in Fig. 5, cell-laden S2A2G2-CC20 bioink (group 1) presents very good cell viability, demonstrating the biocompatibility of the bioink. In contrast, a high number of dead cells is observed when the cell-laden bioink was foamed by the printhead (groups 2 and 3), results being worse for foaming at 2500 versus 1500 rpm. This was expected since higher shear stress is induced at 2500 rpm compared to 1500 rpm. In comparison, there were a higher number of live cells and a lower number of dead cells in the mechanically foamed groups (groups 4 and 5). This indicates that the impact of the foaming process can vary depending on the foaming module and gear design, allowing for optimization based on specific requirements. The internal gear design in the printhead applies higher shear stress due to the bioink being crushed between the teeth of the gears, potentially damaging the cells. However, cell death after mechanical foaming is still significant, even with as low as 10 s (group 4). We therefore decided to avoid cells during foaming and instead add the cells to the foam in a subsequent step. A passive cell mixer was incorporated into the printhead design to mix cells with the foam after the foaming step.

3.7.2. Impact of on-demand foaming speed

A passive cell mixer was incorporated into the printhead design to mix cells with the foam after the foaming step. We then evaluated cell viability in foams produced at different speeds and compared them to non-foam control samples to understand the effects of the foaming process and speed on cell viability. Live/Dead cell assays were performed on four groups of cell-laden grid constructs, as summarized in Table 3: groups 6 and 7, foamed at 1500 and 3500 rpm, respectively, and two control non-foam samples, one with albumin (group 8), one without (group 9). The effect of albumin on cell viability was evaluated between groups 8 and 9. Both control samples were extruded through the printing system without foaming.

Fig. 6a shows the live/dead fluorescent images of control and foam samples on days 1 and 3. In group 6, the cells are observed in two adjacent filaments after 1 day. Similarly, in group 7, cells within two adjacent filaments are observed after both 1 and 3 days. Other images

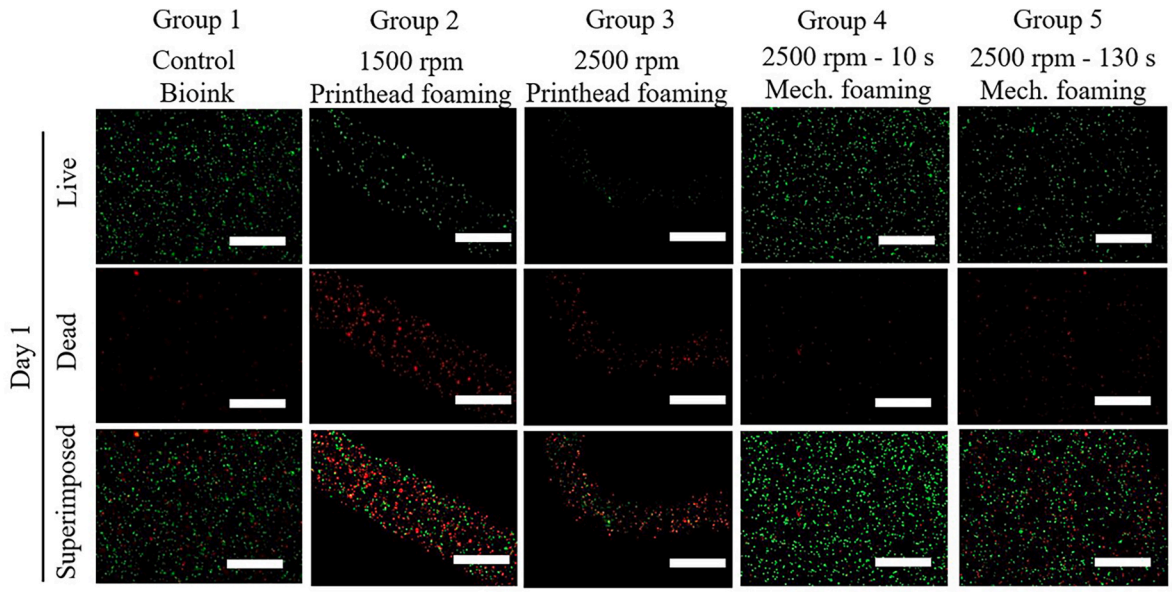

Fig. 5. Fluorescence microscopy images of the cell-laden bioink as the control group, two sample groups foamed with a printhead at 1500 and 2500 rpm, and two sample groups foamed at 2500 rpm with a mechanical mixer at different foaming times after 1 day. (All samples are composed of sodium alginate 2 % w/v, albumin 2 % w/v, and gelatin 2 % w/v. Scale bar: 500 μm).

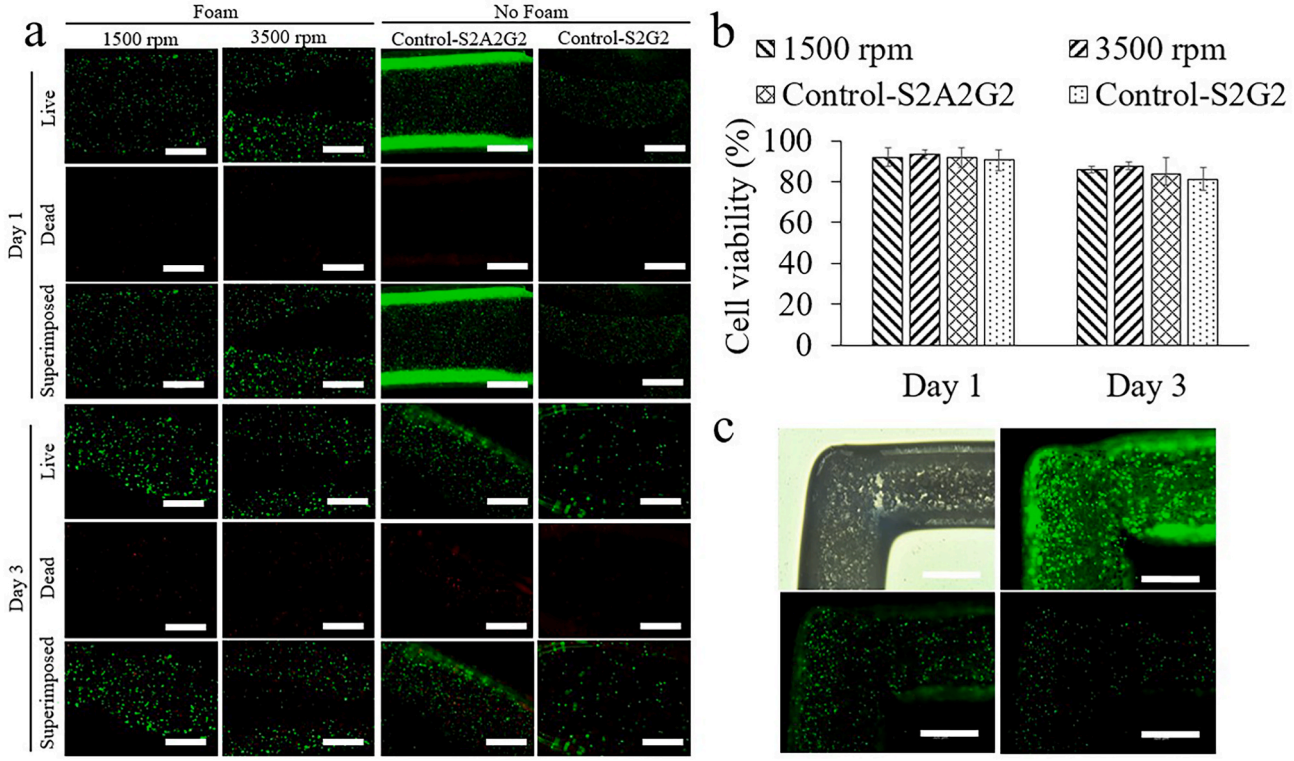

Fig. 6. a) Fluorescence microscopy images and b) cell viability results for foam (S2A2G2-CC20) and control samples after a 3-day cell culture. C) Brightfield and fluorescence microscopy image of the corner of the foam scaffold (1500 rpm) after 1 day. (S: Sodium alginate, A: Albumin, G: Gelatin, scale bar: 500 μm).

show the cells in one filament. The cells are homogenously distributed across all filaments, indicating effective cell suspension and bioink mixing by the mixing module.

The cells maintained high cell viability across all sample groups after 1 and 3 days, demonstrating the biocompatibility of the foam printing system and bioink. Cell viability of over 90.0 % and 80.0 % was observed after 1 and 3 days, respectively, in all samples (Fig. 6b). This is in agreement with the high biocompatibility of sodium alginate, albumin, and gelatin as bioink components in literature [39,40]. The cell viability of 91.9 ± 4.5 %, 93.3 ± 2.0 %, 91.9 ± 4.5 %, and 90.6 ± 5.0 % was observed for study groups of 6–9 after 1 day, respectively.

At the 72 h time point, cell viability remained above 80.0 % in all samples. However, a significant number of cells had left the structure in non-foam samples. The cell viability of 85.7 ± 1.5 %, 87.5 ± 1.9 %, 83.6 ± 8.2 %, and 81.3 ± 5.4 % was observed in foamed samples at 1500 and 3500 rpm, and control samples with albumin and without albumin,

respectively, after 3 days. Cell viability tends to be higher in foam samples (groups 6 and 7) after 3 days compared to non-foam samples (groups 8 and 9). This finding aligns with previous studies comparing porous and bulk hydrogels [28]. More pronounced differences may be observed on larger structures where O_2 and nutrient diffusion to the cells are more problematic. Moreover, cell viability tends to be higher in samples foamed at higher foaming speeds after 3 days. This observation can be due to the increased structural integrity of foams produced at higher speeds and their impact on reducing cell loss. Overall, the results offer insights into the biocompatibility of the on-demand foaming printhead, bioink, and the cell viability range comparable to other 3D bioprinting methods [14,41,40].

While the foaming printhead provides controllable porosity, the foamed constructs are not optically transparent, which may limit compatibility with light-based crosslinking or photopatterning approaches where uniform light penetration is required. This may affect applications involving GelMA or other photocurable bioinks that rely on deep optical curing. Additionally, the present study focused on short-term mechanical and structural characterization; long-term stability, cell-mediated remodeling, and functional performance were not evaluated. Finally, only one polymer formulation was examined, and the generalizability of the foaming strategy to other hydrogel systems remains to be investigated.

The ability to introduce and control porosity during printing has clear practical relevance for tissue engineering applications where mass transport and cellular integration are critical. By adjusting foaming parameters, it becomes possible to print scaffolds with spatial gradients in pore size and stiffness, which could help guide cell migration, support vascular ingrowth, or match the mechanical profile of native tissue interfaces (e.g., muscle–tendon junctions, cartilage–bone transitions). Such porosity gradients can also improve nutrient diffusion and waste removal in thicker constructs, thereby enhancing long-term cell viability and matrix deposition. This highlights the potential of the foaming printhead not only for tuning bulk mechanical properties, but also for engineering scaffolds with spatially defined biological function.

4. Conclusion

In this work, an enclosed foaming printhead was designed and developed to integrate foaming and 3D bioprinting for the creation of heterogeneous supermacroporous structures. The printhead simultaneously mixes the bioink (2 % (w/v) sodium alginate, 2 % (w/v) albumin, 2 % (w/v) gelatin) with air at high speeds during printing, allowing for the adjustment of pore diameter by varying the foaming speed. This printhead demonstrated excellent performance in biofabricating heterogeneous porous constructs, offering promising control over decreasing pore diameter by increasing mixing speed. Several structures were printed using this printhead at various foaming speeds, exhibiting decent layer adhesion, shape fidelity, and high printability number (over 0.9). Characterization of the foams revealed lower water content, degradation, and drug release rates in foams produced at higher speeds. Finally, the designed foaming printhead system allows for mixing cells after foaming and extruding macroporous cell-laden structures with excellent biocompatibility, as demonstrated by high cell viability of L929 fibroblast cells over 3 days. Since this printhead is capable of producing various ranges of pore sizes, it can adapt to the requirements of different targeted cell types and applications. Using foaming speed as a tool to modify metabolic exchange and cell scaffolding properties is preferable and feasible rather than material selection, use of detrimental surfactants, or non-biocompatible processes. Employing this printhead has the potential to mimic the microstructure of human body tissues, such as the hierarchical porous structures.

CRediT authorship contribution statement

Mohammadamin Zohourfazeli: Writing – review & editing, Writing – original draft, Visualization, Validation, Methodology, Investigation, Formal analysis, Data curation, Conceptualization. **Pakshid Hosseinzadeh:** Writing – original draft, Visualization, Validation, Methodology, Formal analysis, Data curation. **Elias Madadian:** Writing – original draft, Methodology, Data curation, Conceptualization. **Sara Badr:** Writing – original draft, Visualization, Validation, Methodology, Formal analysis, Data curation. **Sophie Lerouge:** Writing – review & editing, Writing – original draft, Validation, Supervision, Resources, Project administration, Methodology, Investigation, Funding acquisition, Conceptualization. **Ali Ahmadi:** Writing – review & editing, Writing – original draft, Visualization, Validation, Supervision, Resources, Project administration, Methodology, Investigation, Funding acquisition, Formal analysis, Data curation, Conceptualization.

Declaration of competing interest

The authors declare that they have no known competing financial interests or personal relationships that could have appeared to influence the work reported in this paper.

Acknowledgements

This work was supported by the Natural Sciences and Engineering Research Council of Canada (NSERC) through Discovery Grants RRGPIN-2023-05684 and RGPIN-2020-06684, and by the Canada Foundation for Innovation via the John R. Evans Leader Fund (Project 37696).

Appendix C. Supplementary data

Supplementary data related to this article can be found at https://doi.org/10.1016/j.bprint.2025.e00457.

Data availability

Data will be made available on request.

References

[1] A. Salminen, Increased immunosuppression impairs tissue homeostasis with aging and age-related diseases, J. Mol. Med. 99 (2021) 1–20.
[2] M. Ansari, A. Darvishi, A. Sabzevari, A review of advanced hydrogels for cartilage tissue engineering, Front. Bioeng. Biotechnol. 12 (2024) 1340893.
[3] F.J. Maksoud, et al., Porous biomaterials for tissue engineering: a review, J. Mater. Chem. B 10 (40) (2022) 8111–8165, https://doi.org/10.1039/D1TB02628C, 10.1039/D1TB02628C.
[4] F.J. Maksoud, et al., Porous biomaterials for tissue engineering: a review, J. Mater. Chem. B 10 (40) (2022) 8111–8165.
[5] Z. Zhang, Y. Feng, L. Wang, D. Liu, C. Qin, Y. Shi, A review of preparation methods of porous skin tissue engineering scaffolds, Mater. Today Commun. 32 (2022) 104109, https://doi.org/10.1016/j.mtcomm.2022.104109, 2022/08/01/.
[6] S.S. Lee, X. Du, I. Kim, S.J. Ferguson, Scaffolds for bone-tissue engineering, Matter 5 (9) (2022) 2722–2759.
[7] C.F. Bellani, et al., Suturable elastomeric tubular grafts with patterned porosity for rapid vascularization of 3D constructs, Biofabrication 13 (3) (2021) 035020.
[8] J.L. Hernandez, K.A. Woodrow, Medical applications of porous biomaterials: features of porosity and tissue-specific implications for biocompatibility, Adv. Healthcare Mater. 11 (9) (May 2022) e2102087, https://doi.org/10.1002/adhm.202102087 (in eng).
[9] G. Coste, C. Negrell, S. Caillol, From gas release to foam synthesis, the second breath of blowing agents, Eur. Polym. J. 140 (2020/11/05/2020) 110029, https://doi.org/10.1016/j.eurpolymj.2020.110029.
[10] T. Adachi, et al., Three-dimensional culture of cartilage tissue on nanogel-cross-linked porous freeze-dried gel scaffold for regenerative cartilage therapy: a vibrational spectroscopy evaluation, Int. J. Mol. Sci. 23 (15) (2022) 8099.
[11] E. Bianchi, et al., Gas foamed scaffolds as smart 3D structures in skin tissue engineering, J. Drug Deliv. Sci. Technol. 95 (2024) 105541.
[12] C. Wang, Y. Zhou, Sacrificial biomaterials in 3D fabrication of scaffolds for tissue engineering applications, J. Biomed. Mater. Res. B Appl. Biomater. 112 (1) (2024) e35312.
[13] R. Foudazi, R. Zowada, I. Manas-Zloczower, D.L. Feke, Porous hydrogels: present challenges and future opportunities, Langmuir 39 (6) (2023/02/14 2023) 2092–2111, https://doi.org/10.1021/acs.langmuir.2c02253.

[14] Z.-X. Chen, X.-J. Zha, Y.-K. Xia, T.-X. Ling, J. Xiong, J.-G. Huang, 3D foaming printing biomimetic hierarchically macro–micronanoporous hydrogels for enhancing cell growth and proliferation, ACS Appl. Mater. Interfaces 16 (8) (2024) 10813–10821.
[15] A.-L. Fameau, S. Fujii, Stimuli-responsive liquid foams: from design to applications, Curr. Opin. Colloid Interface Sci. 50 (2020/12/01/2020) 101380, https://doi.org/10.1016/j.cocis.2020.08.005.
[16] R. Deleurence, T. Saison, F. Lequeux, C. Monteux, Foaming of transient polymer hydrogels, ACS Omega 3 (2) (2018/02/28 2018) 1864–1870, https://doi.org/10.1021/acsomega.7b01301.
[17] J. Liu, Z. Zheng, J. Luo, P. Wang, G. Lu, J. Pan, Engineered reversible adhesive biofoams for accelerated dermal wound healing: intriguing multi-covalent phenylboronic acid/cis-diol interaction, Colloids Surf. B Biointerfaces 221 (2023) 112987, https://doi.org/10.1016/j.colsurfb.2022.112987, 2023/01/01/.
[18] M. Shahrousvand, N.G. Ebrahimi, H. Oliaie, M. Heydari, M. Mir, M. Shahrousvand, Chapter 4 - polymeric transdermal drug delivery systems, in: A.T. Azar (Ed.), Modeling and Control of Drug Delivery Systems, Academic Press, 2021, pp. 45–65.
[19] X. Xu, et al., Applications of human and bovine serum albumins in biomedical engineering: a review, Int. J. Biol. Macromol. (2023) 126914.
[20] Y. Fang, et al., Expanding embedded 3D bioprinting capability for engineering complex organs with freeform vascular networks, Adv. Mater. 35 (22) (2023) 2205082, https://doi.org/10.1002/adma.202205082.
[21] R. Hasanzadeh, T. Azdast, M. Mojaver, M.M. Darvishi, C.B. Park, Cost-effective and reproducible technologies for fabrication of tissue engineered scaffolds: the state-of-the-art and future perspectives, Polymer 244 (Feb. 2022) 124681, https://doi.org/10.1016/j.polymer.2022.124681.
[22] T. Azdast, R. Hasanzadeh, Polylactide scaffold fabrication using a novel combination technique of fused deposition modeling and batch foaming: dimensional accuracy and structural properties, Int. J. Adv. Manuf. Technol. 114 (5) (Mar. 2021) 1309–1321, https://doi.org/10.1007/S00170-021-06915-9, 2021 114:5.
[23] S. Aghaiee, T. Azdast, R. Hasanzadeh, F. Farhangpazhouh, Fabrication of bone tissue engineering scaffolds with a hierarchical structure using combination of 3D printing/gas foaming techniques, J. Appl. Polym. Sci. 141 (16) (Apr. 2024) e55238.
[24] S.Y. Jo, J.U. Lee, H. Lee, D. Ryu, G.H. Kim, The one-step fabrication of porous hASC-laden GelMa constructs using a handheld printing system, NPJ Regen. Med. 8 (1) (Jun. 2023) 1–16, https://doi.org/10.1038/s41536-023-00307-1, 2023 8:1.
[25] F. Saeedinejad, et al., In situ-formed tissue-adhesive macroporous scaffolds enhance cell infiltration and tissue regeneration, Acta Biomater. 200 (Jun. 2025) 358–377, https://doi.org/10.1016/J.ACTBIO.2025.04.049.
[26] A. Seyedsalehi, et al., Benefits of in situ foamed and printed porous scaffolds in wound healing, Adv. Healthcare Mater. 13 (31) (Dec. 2024) 2401944, https://doi.org/10.1002/ADHM.202401944.
[27] E. Madadian, E. Naseri, R. Legault, A. Ahmadi, Development of 3D-Printable albumin–alginate foam for wound dressing applications, 3D Print. Addit. Manuf. 11 (3) (2024) e1175–e1185.
[28] A. Mostafavi, et al., Colloidal multiscale porous adhesive (bio) inks facilitate scaffold integration, Appl. Phys. Rev. 8 (4) (2021).
[29] J. Condi Mainardi, et al., 3D bioprinting of hydrogel/ceramic composites with hierarchical porosity, J. Mater. Sci. 57 (5) (2022) 3662–3677, https://doi.org/10.1007/s10853-021-06829-7, 2022/02/01.
[30] S. Badr, et al., Development of a mist-based printhead for droplet-based bioprinting of ionically crosslinking hydrogel bioinks, Bioprinting 27 (2022/08/01/2022) e00207, https://doi.org/10.1016/j.bprint.2022.e00207.
[31] L. Ouyang, R. Yao, Y. Zhao, W. Sun, Effect of bioink properties on printability and cell viability for 3D bioplotting of embryonic stem cells, Biofabrication 8 (3) (2016) 035020.
[32] A. Ribeiro, et al., Assessing bioink shape fidelity to aid material development in 3D bioprinting, Biofabrication 10 (1) (2017/11/30 2018) 014102, https://doi.org/10.1088/1758-5090/aa90e2.
[33] A.M. Hawkins, T.A. Milbrandt, D.A. Puleo, J.Z. Hilt, Composite hydrogel scaffolds with controlled pore opening via biodegradable hydrogel porogen degradation, J. Biomed. Mater. Res. 102 (2) (2014) 400–412, https://doi.org/10.1002/jbm.a.34697.
[34] E. Madadian, S. Badr, D.S. MacDonald, R.A. Tasker, A. Ahmadi, Development of foam-based support material for coaxial bioprinting of ionically crosslinking bioinks, Bioprinting 32 (2023/07/01/2023) e00281, https://doi.org/10.1016/j.bprint.2023.e00281.
[35] N.L. Davison, F. Barrère-de Groot, D.W. Grijpma, Degradation of biomaterials, Tissue Eng. (2014) 177–215.
[36] Z. Chen, Y. Lv, Gelatin/sodium alginate composite hydrogel with dynamic matrix stiffening ability for bone regeneration, Compos. B Eng. 243 (2022/08/15/2022) 110162, https://doi.org/10.1016/j.compositesb.2022.110162.
[37] J. Lee, H. Lee, E.-J. Jin, D. Ryu, G.H. Kim, 3D bioprinting using a new photo-crosslinking method for muscle tissue restoration, NPJ Regen. Med. 8 (1) (2023) 18, https://doi.org/10.1038/s41536-023-00292-5, 2023/03/31.
[38] A.C. Daly, S.E. Critchley, E.M. Rencsok, D.J. Kelly, A comparison of different bioinks for 3D bioprinting of fibrocartilage and hyaline cartilage, Biofabrication 8 (4) (2016/10/07 2016) 045002, https://doi.org/10.1088/1758-5090/8/4/045002.
[39] A.K. Singh, K. Pramanik, A. Biswas, Constructing a biofunctionalized 3D-printed gelatin/sodium alginate/chitosan tri-polymer complex scaffold with improvised biological and mechanical properties for bone-tissue engineering, Bio-Design and Manufacturing 7 (1) (2024) 57–73.
[40] Y. Koo, G. Kim, An approach for fabricating hierarchically porous cell-laden constructs utilizing a highly porous collagen-bioink, Adv. Funct. Mater. (2024) 2316222.
[41] E. Madadian, H. Ravanbakhsh, F. Touani Kameni, M. Rahimnejad, S. Lerouge, A. Ahmadi, In-Foam bioprinting: an embedded bioprinting technique with self-removable support Bath, Small Science (2024) 2300280.